UCLA
UCLA Previously Published Works

Title
MS-STEM-FEM: A parallelized multi-slice fluctuation TEM simulation tool.

Permalink
https://escholarship.org/uc/item/4v7486g2

Authors
Julian, Nicholas H
Li, Tian T
Rudd, Robert E
et al.

Publication Date
2018-11-01

DOI
10.1016/j.ultramic.2018.08.001

Peer reviewed

eScholarship.org Powered by the California Digital Library
University of California

Ultramicroscopy 194 (2018) 117–125

Contents lists available at ScienceDirect

Ultramicroscopy

journal homepage: www.elsevier.com/locate/ultramic

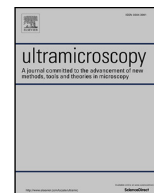

MS–STEM–FEM: A parallelized multi-slice fluctuation TEM simulation tool

Nicholas H. Julian*[,a,b], Tian T. Li[b], Robert E. Rudd[b], Jaime Marian[a,c]

[a] Department of Materials Science and Engineering, University of California, Los Angeles, CA 90095 USA
[b] Lawrence Livermore National Laboratory, Livermore, CA 94551 USA
[c] Department of Mechanical and Aerospace Engineering, University of California, Los Angeles, CA 90095 USA

ARTICLE INFO

Keywords:
Fluctuation microscopy
Multislice simulation
Medium-range order
Amorphous

ABSTRACT

Atomic configurations of glassy or amorphous materials containing medium-range order (MRO) may be identified by comparing fluctuation transmission electron microscopy (FTEM) measurements to FTEM simulations obtained using model configurations. Candidate model sizes have traditionally been much thinner than the samples measured experimentally, and publicly available FTEM simulation software has until now omitted microscope parameters, dynamical scattering, and the phase of the diffracted electron wave. We introduce MS–STEM–FEM, an open-source software package for simulating FTEM experiments using established multislice TEM simulation techniques to emulate experiment more closely by incorporating microscope parameters and simulating electron scattering and propagation as a complex valued wave. Simulations using established models are compared with results of experimental STEM–FEM to validate the software. Several statistical measures of diffraction are implemented and their responses to model features are compared. Dynamical scattering is found to be less influential than the variety of crystallite orientations which occur in thicker models. Simulations of variable resolution microscopy confirm that cumulative intensity of the FTEM signal decreases with reduced model MRO and increased coherence volume. Advantageous model scaling characteristics and efficient processor performance scaling are demonstrated, along with a study of convergence with respect to pertinent simulation parameters to identify accuracy requirements.

1. Introduction

Fluctuation transmission electron microscopy (FTEM) is an experimental technique for characterizing medium-range order (MRO) in glassy or amorphous materials. The occurence of nanoscale crystalline regions in otherwise amorphous materials has been observed to induce spatially fluctuating speckle in electron diffraction patterns. FTEM uses statistical analysis of the fluctuations to quantify the medium-range order. Correlating atomic configurations with FTEM measurements may enable computational investigations of technologically important properties of medium-range ordered materials. Accurate simulations of the FTEM experiment are desired to identify configurations which match experimental data, enabling further investigations and a deeper understanding of the properties of materials having medium-range order. STEM–FEM is a technique for performing FTEM by rastering the probe in a nano-beam diffraction measurement. The MS–STEM–FEM software package introduced here is designed to simulate STEM–FEM measurements taken in a nano-diffraction setting using a well-established multi-slice scanning transmission electron microscopy (STEM) simulation technique which enables incorporation of instrument parameters and accommodates samples of various composition and size to accurately represent experimental conditions and procedure.

1.1. Fluctuation transmission electron microscopy

Fluctuation transmission electron microscopy uses statistical measures of electron diffraction to characterize MRO in materials. Many glassy and amorphous materials of industrial importance lack long-range order and have atomic configurations which may otherwise appear random but give rise to speckled diffraction patterns which are noticeably distinguishable from the isotropic diffraction patterns of truly disordered materials. MRO is an ordering at the scale beyond nearest neighbors, on the 1–3 nm scale, which the pair correlation function $g(r)$ is insufficiently sensitive to characterize [1,2]. FTEM arose as a consequence of the idea that limiting the coherence volume of the impingent electron beam would suppress diffraction from long-range order while enhancing diffraction from pair-pair correlations and medium-range order [3,4].

* Corresponding author at: Department of Materials Science and Engineering, University of California, Los Angeles, CA 90095 USA.
E-mail address: njulian@ucla.edu (N.H. Julian).

https://doi.org/10.1016/j.ultramic.2018.08.001
Received 16 May 2018; Received in revised form 26 July 2018; Accepted 1 August 2018
Available online 02 August 2018
0304-3991/ © 2018 Elsevier B.V. All rights reserved.

Nano-beam diffraction in a TEM uses beam convergence to tune the size of the coherent beam and limit the sample volume which contributes to diffraction. Tuning a nano-beam size to the MRO scale and rastering it across a material sample is a convenient way to obtain spatial ensembles of limited-coherence-volume diffraction from which statistical measures may be calculated [2,5]. This procedure is sometimes referred to as STEM–FEM.

1.2. FTEM simulation

Identifying atomic configurations which reproduce FTEM signals is desirable so that their properties and behavior may be predicted. Direct inversion from FTEM measurement to atomic configuration is not possible with current computational capabilities. Instead, a forward calculation of FTEM from candidate atomic configurations has proven useful in constructing configurations which match experiment [6].

The available software for simulating FTEM from atomic configuration (FEMSIM) uses a kinematic diffraction approximation, wherein the entire sample is projected into a single two-dimensional plane [7]. In the projected calculation, each atomic pair within a designated cutoff distance produces a real-valued diffraction intensity proportional to the product of two Airy discs and a first-order Bessel function. These real-valued diffraction components are calculated for each contributing reciprocal space vector and summed together. Summing real-valued diffraction contributions, omitting the wave phase encoded in complex values, loses information about the limited coherence volume which originally motivated FTEM method development [4]. Model size (including thickness) is notably limited in FEMSIM because calculations scale quadratically with the number of atoms [6].

It has been shown that microscope variation and sample thickness contribute significantly to STEM–FEM measurements [8]. It follows that an approach of simulating the microscope beam and experimental procedure is an appealing means of including influential non-idealities into FTEM simulations. MS–STEM–FEM adapts existing multi-slice TEM simulation methods to achieve these abilities in an FTEM simulation which scales well to larger model sizes.

2. Theory and implementation

MS–STEM–FEM follows the multi-slice algorithms, formulas, and parameter fittings detailed in the publications of Kirkland to simulate the beam and material interaction in a STEM [9,10]. In the following, we discuss the theoretical underpinnings of the method and give details about its implementation.

2.1. Multi-slice method

The multi-slice method approximates a material sample as a series of two-dimensional projected atomic potentials separated by free space. The atomic potentials have been tabulated for all of the common elements [9]. A complex valued probe wave function is repeatedly modified by the projected atomic potentials and propagated over their separating distances until exiting the sample.

The nano-beam probe is initialized at the origin $\vec{r_p} = 0$ as a functional of objective lens aberration $\chi(\|\vec{k}\|)$ and probe-forming aperture function $A(\|\vec{k}\|)$

$$\Psi_p(\vec{r}, \vec{r_p}) = A_p \mathcal{F}^{-1}[e^{-i(\chi(\|\vec{k}\|)+2\pi i \vec{k}\cdot\vec{r_p})} A(\|\vec{k}\|)] \tag{1}$$

$$\chi(\|\vec{k}\|) = \begin{cases} \pi\lambda\|\vec{k}\|^2\left(\frac{1}{2}C_{s3}\lambda^2\|\vec{k}\|^2 - \Delta f\right) & \text{w/o aberration correction} \\ \pi\lambda\|\vec{k}\|^2\left(\frac{1}{2}C_{s3}\lambda^2\|\vec{k}\|^2 + \frac{1}{3}C_{s5}\lambda^4\|\vec{k}\|^4 - \Delta f\right) & \text{with aberration correction} \end{cases} \tag{2}$$

$$A(\|\vec{k}\|) = \begin{cases} 1 & \|\vec{k}\| < Q = \frac{\alpha_{max}}{\lambda} \\ 0 & \text{otherwise} \end{cases} \tag{3}$$

where A_p is a normalization factor such that $\|\sum_{\vec{r}} \Psi_p(\vec{r}, \vec{r_p})\| = 1$, $\mathcal{F}^{-1}$ is the inverse Fourier transform, Δf is microscope defocus, C_{s3} and C_{s5} are the third and fifth order spherical lens aberrations, λ is electron wavelength evaluated from the microscope accelerating potential, and $\alpha_{\max}$ is the maximum beam convergence angle. When the beam raster position shifts, a copy of these real space values is translated to be centered at the pixel nearest the raster position and transformed to reciprocal space via inverse FFT.

Interaction of the beam with the sample follows a weak phase approximation in which atoms are represented by two-dimensional potentials projected onto the top of each slice, the thickness of which is tunable by a run-time parameter. After domain discretization, the position of each atom is shifted to a pixel nearest their true positions to ensure that the point of maximum atomic potential is not omitted and the discretized values of each atom's potential are centro-symmetric about their maxima. The projected atomic potential $v_{nz}(x, y)$ of the nth slice, containing atoms indexed by j, is evaluated as

$$v_{nz}(x, y) = \mathcal{F}^{-1}[V_{nz}(k_x, k_y, 0)] \tag{4}$$

$$\sigma V_{nz}(k_x, k_y, 0) = \lambda\gamma\frac{1}{L_x L_y}\sum_j f_{ej}(k_x, k_y, 0)\exp[2\pi i(k_x x_j + k_y y_j)] \tag{5}$$

$$f_e(k_x, k_y) = \sum_{i=1}^{3}\frac{a_i}{k_x^2 + k_y^2 + b_i} + \sum_{i=1}^{3} c_i \exp[-d_i(k_x^2 + k_y^2)] \tag{6}$$

where f_{ej} is the jth atomic scattering factor with fitted parameters a_i, b_i, c_i, d_i adopted from [9], L_x and L_y are lateral material dimensions, and γ is the Lorentz factor of the impingent electrons. The beam wave function interacts with a slice's projected atomic potential via the transmission function t_n implemented as [10]

$$t_n(x, y) = 1 + i\sigma v_{nz}(x, y) \tag{7}$$

$$\sigma = \frac{2\pi}{\lambda V}\left(\frac{m_0c^2 + eV}{2m_0c^2 + eV}\right) \tag{8}$$

After interacting with a slice's transmission function, the beam wave function is propagated over the slice thickness Δz by reciprocal space multiplication with the slice's propagator function P_n

$$\psi_{n+1}(k_x, k_y) = P_n(k_x, k_y, \Delta z_n)\mathcal{F}[t_n(x, y)\psi_n(x, y)] \tag{9}$$

$$P_n(k_x, k_y, \Delta z_n) = \exp[-i\pi\lambda(k_x^2 + k_y^2)\Delta z_n] \tag{10}$$

To avoid aliasing effects of using the FFT as an alternative to real-space convolution, the wave function is bandwidth limited to spatial frequencies of magnitude less than 2/3 the maximum spatial frequency of the shortest lateral dimension after each forward Fourier transform. The projected atomic potential is bandwidth limited to 1/2 the maximum spatial frequency of the shortest lateral dimension.

After interacting with the propagator of the lower-most slice, the diffracted intensity takes the form of the magnitude of the beam wave function in reciprocal space,

$$I(\vec{k}, \vec{r_p}) = \|\psi_{\text{final}}(k_x, k_y)\| \tag{11}$$

As of this writing the FTEM measures calculated by MS–STEM–FEM do not include possible non-idealities of an instrument's detector, such as random noise or non-linear signal response.

2.2. Extension to fluctuation TEM

Several statistical measures based on the computed diffracted intensity have been implemented. The conventional measure of medium-

range order in FTEM is the *normalized variance of the annular mean* $V_\Omega(k)$ given by Eq. (12). Additional measures investigated by Daulton *et al.* which encapsulate different but potentially useful information include the *normalized variance of ring ensembles* V_{re} (Eq. (13)), *mean of normalized variances of rings* $\overline{V_r}$ (Eq. (14)), and the *annular mean of variance image* Ω_{VImage} (Eq. (15)) , each of which may be computed from the same collection of diffraction images.

$$V_\Omega(\|\vec{k}\|) = \frac{\langle\langle I(\vec{k},\vec{r})\rangle_\phi^2\rangle_{\vec{r}}}{\langle\langle I(\vec{k},\vec{r})\rangle_\phi\rangle_{\vec{r}}^2} - 1 \quad (12)$$

$$V_{re}(\|\vec{k}\|) = \frac{\langle I^2(\vec{k},\vec{r})\rangle_{\vec{r},\phi}}{\langle I(\vec{k},\vec{r})\rangle_{\vec{r},\phi}^2} - 1 \quad (13)$$

$$\overline{V_r}(\|\vec{k}\|) = \left\langle \frac{\langle I^2(\vec{k},\vec{r})\rangle_\phi}{\langle I(\vec{k},\vec{r})\rangle_\phi^2} - 1 \right\rangle_{\vec{r}} \quad (14)$$

$$\Omega_{VImage}(\|\vec{k}\|) = \left\langle \frac{\langle I^2(\vec{k},\vec{r})\rangle_{\vec{r}}}{\langle I(\vec{k},\vec{r})\rangle_{\vec{r}}^2} - 1 \right\rangle_\phi \quad (15)$$

We use the notation in which angled brackets $< \cdot >_x$ represent averaging of the enclosed function over the subscripted variable x, and ϕ is the azimuthal angle of reciprocal space vector $\vec{k}$. Note that the statistical measure used by Gibson and Treacy [11] closely approximates $\Omega_{VImage}(\|\vec{k}\|) + 1$.

2.3. Algorithm summary

MS–STEM–FEM assembles the methods of Sections 2.1 and 2.2 into the following procedure:

1. Initialize discretized domains split over all compute nodes via MPI
2. Initialize nano-beam probe (Eq. (1))
3. Initialize a look-up-table containing projected atomic potential values (Eq. (4)) for each unique atomic species
4. Divide the model into slices having minimum thickness specified by the user
5. Initialize transmission function for each slice (Eq. (7)) on the local node's spatial domain
6. Accumulate a total projected atomic potential (Eq. (5)) for each slice, re-centering values of the look-up-table to the pixel nearest each corresponding atomic position
7. For each rastering position separated by a user-specified value,
   (a) Create translated nano-beam wave function values $\psi(x, y) \in \mathbb{C}$ centered at the pixel nearest the rastering position $\vec{r_p}$
   (b) For each slice of the model recursively transmit and propagate the beam wave function so that upon exiting the nth slice it will be

$$\psi_{n+1} = \mathcal{F}^{-1}[P_n(k_x, k_y, \Delta z_n)\mathcal{F}[t_n(x, y)\psi_n(x, y)]] \quad (16)$$

   (c) Depending upon requested FTEM measurement quantities, calculate and accumulate diffraction intensity quantities for FTEM measures
8. Finalize calculations of FTEM measures using Eqs. (12)–(15) and save output to text, image, and/or netCDF files

2.4. Implementation

MS–STEM–FEM is written in C+ + with MPI and released under the GNU Public License version 2 [12,13]. The program is parallelized by splitting the beam wave-function and material sample properties among processors along a direction perpendicular to beam propagation. The FFTW fast Fourier transform (FFT) library is used to transform the propagating wave function between real and reciprocal space as needed to efficiently calculate convolutions [14]. Use of the discrete FFT induces periodic boundary conditions and aliasing effects which we eliminate with bandwidth limiting.

2.5. Construction of models from smaller configurations

Use of established models eases comparison to existing simulation results, but the majority of available models are not sufficiently large to obtain comparible resolution in reciprocal space. To obtain a discretized spacing Δk in reciprocal space comparable to experimental data, the dimensions of a model with periodic boundary conditions must be at least $(\Delta k)^{-1}$. Imitation of experiment also imposes a minimum on the model dimension, which we take to be the product of the number of probe raster positions and their average separation. To approach these dimensions we extend existing models using a method similar to the stacking method of Bogle et al. [15]. The model extension method used in the following sections duplicates a model $N_x \times N_y \times N_z$ times as follows:

1. For each layer 1,...,N_z
   (a) For each of the $N_x \times N_y$ sub-cells
      (i) duplicate the basis atom positions into a 3 × 3 × 3 grid
      (ii) choose a rotation by uniformly sampling the special orthogonal group of three dimensional rotations, $SO(3)$, and apply the rotation to the positions of the 3 × 3 × 3 grid about its center
      (iii) delete all atoms from the reoriented 3 × 3 × 3 grid which exceed the bounds of the original smaller model
   (b) choose a uniformly distributed lateral translation of magnitude less than half the width of the basis model and translate the entire layer by that amount subject to periodic boundary conditionsFig. 1 shows the paracrystalline basis models used

and an example of a paracrystalline model extension in which the cubic diamond atoms and their bonds are highlighted in blue, while the atoms approximating a continuous random network are colored in red. These basis models were chosen from the work of Bogle et al. and are referred to by the number of atoms in their crystallites (*e.g.* 163g123g87g59g has four crystallites containing 163, 123, 87, and 59 atoms, respectively, surrounded by a continuous random network). For a detailed explanation of their construction see Ref. [15]. The impact of the lateral periodicity between crystallites is unclear but could contribute to spatial frequencies near or below that of the periodicity, being $(27\ \text{Å})^{-1} = 0.037\ \text{Å}^{-1}$.

3. Results and discussion

3.1. Comparison of simulations to experiment

To validate the MS–STEM–FEM software we compare V_Ω from MS–STEM–FEM simulations to experimental STEM–FEM results of amorphous Germanium (a-Ge). Experimental STEM–FEM measurements were adapted from Ref. [16], in which a 33 nm thick a-Ge film was sputtered onto an approximately 20 nm thick amorphous silicon nitride (SiN_x) membrane. The experimental data set contains measurements from five regions. Existing paracrystalline models of a-Si from Ref. [15] were dilated to match Ge lattice parameters and then extended into a 4 × 4 × 12 grid using the method outlined in the previous section to have dimensions of 11 × 11 × 33 nm^3, similar in thickness to that of the experimentally measured a-Ge but an order of magnitude smaller than the experiment in each of the probed surface dimensions. The basis models were chosen for their demonstrated ability to produce a simulated V_Ω signal worthy of comparison to experiment. Ten paracrystalline model extensions constructed by the

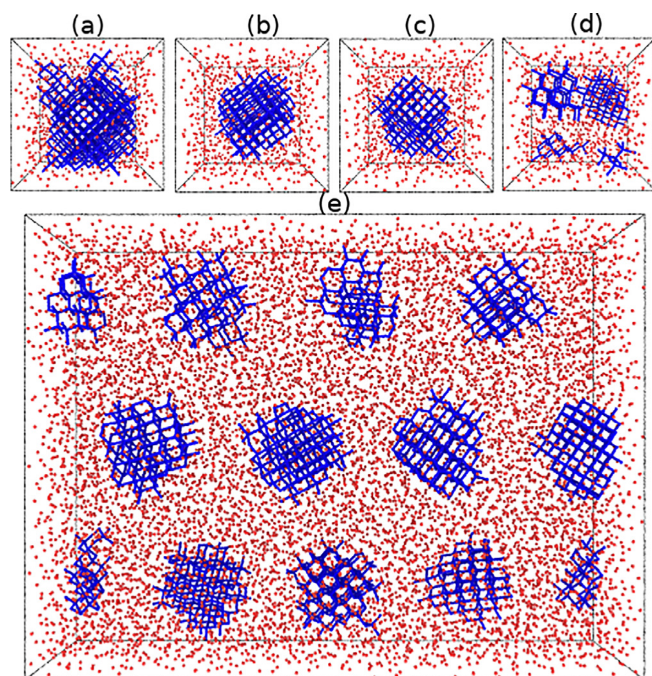

Fig. 1. Paracrystalline basis models and a model extension showing the bonds and atoms of cubic diamond arrangements in blue, and the approximate continuous random network atoms in red. (a) 429g, (b) 317g, (c) 211g, (d) 163g123g87g59g, and (e) 429g_4 × 1 × 3 extension. (For interpretation of the references to colour in this figure legend, the reader is referred to the web version of this article.)

method detailed in Section 2.5 were simulated for each smaller basis model. Model names indicate the number of atoms in the crystallite regions of each model and the number of times it was duplicated in each dimension. For example, 211g_4 × 4 × 12 contains one grain of 211 atoms surrounded by a continuous random network duplicated 4 times in the lateral directions and 12 times in the beam propagation direction with rotations and translations as detailed in Section 2.5. Additionally, a continuous random network (CRN) model was adapted from the work of Barkema and Mousseau [17]. This model of 100,000 Si atoms was scaled to match Ge, extended using the method of the Section 2.5 into ten larger models, and then trimmed to have a thickness similar to that of the experimental a-Ge film. Unless otherwise specified, both experiment and simulation used a convergence angle of 1.0 mRad and a 10 × 10 raster of 100 points. This was obtained by a raster spacing of 10 nm in the experiments and 1.1 nm in the simulations. The shared convergence angle yielded a measured probe full-width at half maximum (FWHM) of 2.0 ± 0.1 nm in the experiment and 1.7 nm in the simulation.

Average V_{Ω} values from both experiment and simulation are plotted in Fig. 2 as solid curves surrounded by shaded regions representing one standard deviation of the values obtained from several models or regions measured. No single simulated V_{Ω} curve matched an experimental V_{Ω} curve especially well, so we instead present the averages and standard deviations derived from multiple models and experiments. Fig. 2(b) represents data previously published by Li et al. [16] wherein standard error is presented rather than the standard deviation shown here.

The shaded regions of Fig. 2(a) indicate that a single small model may yield a wide range of V_{Ω} values dependent upon the orientations of its duplicates in the paracrystalline extensions. This sensitivity is a testament to the ability of V_{Ω} to distinguish between configurations.

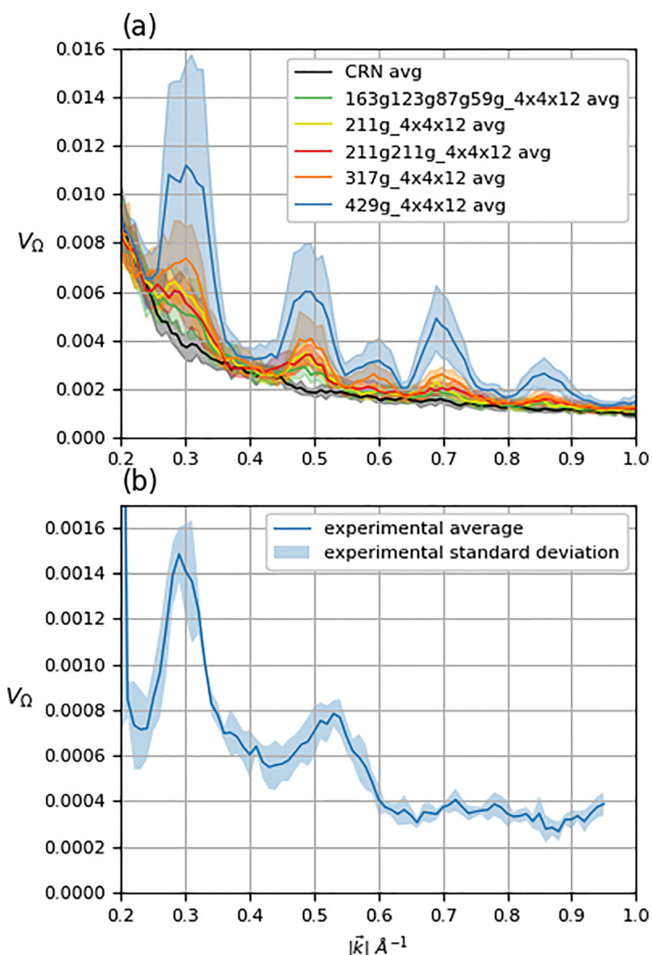

Fig. 2. (a) Averaged V_{Ω} calculated over several paracrystalline Ge models, and (b) average V_{Ω} of experimental STEM–FEM measurement. The experimental data were previously reported in Ref. [16]. Shaded regions represent one standard deviation from the average (solid curve) calculated from ten model extensions in (a) and five material regions in (b). (For interpretation of the references to colour in this figure legend, the reader is referred to the web version of this article.)

The number of peaks and their positions in the average simulated V_{Ω} shown in Fig. 2(a) are in fair agreement with simulations reported in Ref. [15]. Comparison among the average values of V_{Ω} in Fig. 2(a) shows that the models having larger crystalline regions (429g_4 × 4 × 12) have greater peak intensities and peak ratios which more closely resemble the average experimental curve.

The experimental V_{Ω} values are nearly an order of magnitude smaller than our simulated V_{Ω}. A similar disparity also occurs in kinematical scattering simulations for which Rezikyan et al. have proposed atomic displacement decoherence as an important contribution [18]. Also, exclusion of the SiN_x substrate from our models introduces a difference in thickness which would enhance the simulated V_{Ω} magnitude through an inverse proportionality as demonstrated by Yi and Voyles [19].

Positions and relative heights of the peaks below 0.6 $Å^{-1}$ are in fair agreement between the experiment and simulation averages, with the simulation having a red-shift in the peak near 0.5 $Å^{-1}$. However, notable differences between the experiments and these models occur for values at or above 0.6 $Å^{-1}$, where the models produce several peaks which are not significantly pronounced in the experiment. Peaks at

these locations are common to the output of both MS–STEM–FEM and FEMSIM when using these basis models [15] suggesting a need to improve our model construction method. Absence of the amorphous SiN_x substrate from our models and may also contribute to these differences between simulated and experimental V_Ω peaks.

3.2. Comparison of statistical measures

Insight into the sensitivity to model variation of the statistical measures outlined in Eqs. (12)–(15) may be gained by comparing trends in their values. Fig. 3 shows the average and standard deviation of each statistical measure calculated from ten extensions of the CRN model and ten extensions of each of three paracrystalline models of increasing % crystallinity. Peak position and shape are similar between $\overline{V}_r$ and V_{re}, suggesting that they contain redundant information . V_Ω is the only measure which appears to be superimposed upon the tail of a decaying lower frequency peak, which makes it difficult to distinguish low amplitude peaks in the range of MRO, especially for the models having lower % crystallinity.

Examining the standard deviations of these statistical measures, shown as shaded regions, shows relative variations among model extensions derived from the same crystallite model are greater in V_Ω than in $\overline{V}_r$, V_{re}, and Ω_{VImage}. Points indicating all local maxima in the ten curves of 429g models are overlaid upon the average curves to emphasize that peak positions vary most for V_Ω. This measure is then better suited to distinguish between paracrystalline constructions which use a single crystallite. However, the peaks in V_Ω for models with lower % crystallinity may be more difficult to discern from the CRN model curve than the other measures, in part because the statistical deviations of V_Ω are larger over each set of models.

3.3. Variable resolution simulation

Relating the statistical measurements of diffraction in FTEM to a property that is easier to physically visualize such as % crystallinity has been a recurring theme in FTEM. Several studies have identified that reducing the coherence volume of the electron beam enhances V_Ω for samples having medium-range order on the scale of the coherence volume [3,20,21]. This method of measuring $V_\Omega(\|\vec{k}\|, Q)$ as a function of both aperture and wavevector in a STEM is referred to as variable resolution microscopy. To confirm that the multislice method and STEM–FEM agree with this notion, fluctuation maps for several models are shown in Fig. 4 where we use the beam probe diameter (FWHM) as a surrogate for Q.

A few features of Fig. 4 are worth noting. In STEM–FEM experiments on a sample of uniform thickness, coherence volume is tuned by varying the beam probe FWHM, which is inversely proportional to Q or $\alpha_{\max}$ (Eq. (1)) and thus also the diffracted disc diameter. The dark regions in the lower left of each plot are the locations of the direct beam diffraction disc, showing the inverse proportionality in width to the probe FWHM. The width of peaks in V_Ω are visibly similar to the radius of the direct beam disc, and overlap when their separation is less than twice the diffraction disc radius. Overlapping diffraction discs result in peaks in V_Ω which may not have previously been properly attributed, since they do not align directly with reciprocal lattice vectors of the crystallites.

Fig. 5 illustrates the reduction in cumulative V_Ω for models of reduced medium-range order, and enhancement for lower coherence volumes. There is no notable local maximum in intensity when the probe diameter is similar to crystallite diameters as may have been suggested previously [21]. However, some notable resonance does

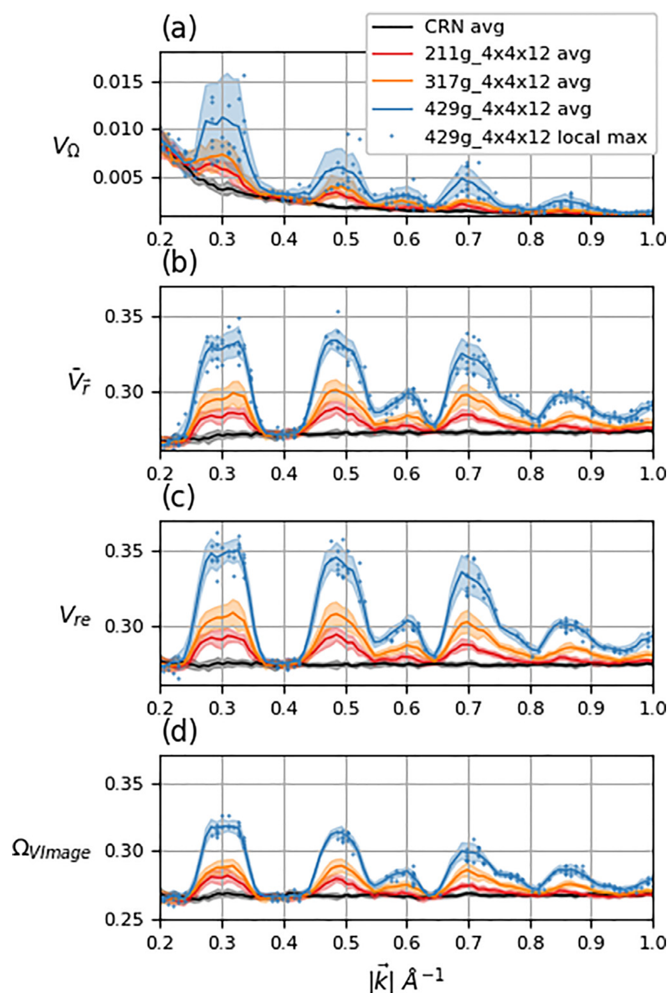

Fig. 3. Comparison of statistical measures (Eqs. (12)–(15)) derived from STEM–FEM simulations. Average values (solid curves) surrounded by shaded regions of one standard deviation among ten model extensions show sensitivity of each measure to crystallinity and crystallite orientation. Local maxima of curves calculated from the paracrystalline model of greatest % crystallinity (429g_4 × 4 × 12) are identified as points to illustrate variations in peak position. (For interpretation of the references to colour in this figure legend, the reader is referred to the web version of this article.)

occur in Fig. 4 near 0.22 Å^{-1} for the model of greatest % crystallinity having crystallite diameter of nearly 25 Å, 429g_4 × 4 × 12_01, and this produces a single peak in the cumulative V_Ω of Fig. 5 for a probe size of less than 5 Å. Except for this point, a small probe is not shown to yield local peaks in intensity for correspondingly smaller crystallites for these models in STEM–FEM. Instead, the total intensity of V_Ω decreases with increasing probe size nearly monotonically, where additional exceptions are due to rectangular harmonics appearing in the shape of the larger probes due to periodic boundary conditions.

Periodic boundary conditions have a detrimental effect on probe shape when its size approaches approximately one sixth of the width of the domain, inducing non-circular probe shapes which modify the diffracted intensities. Horizontal stripes of reduced intensity in Fig. 4 and 5 (*e.g.* near FWHM ≈20 Å and 40 Å) are due to these artifacts in the probe shape.

 Ultramicroscopy 194 (2018) 117–125

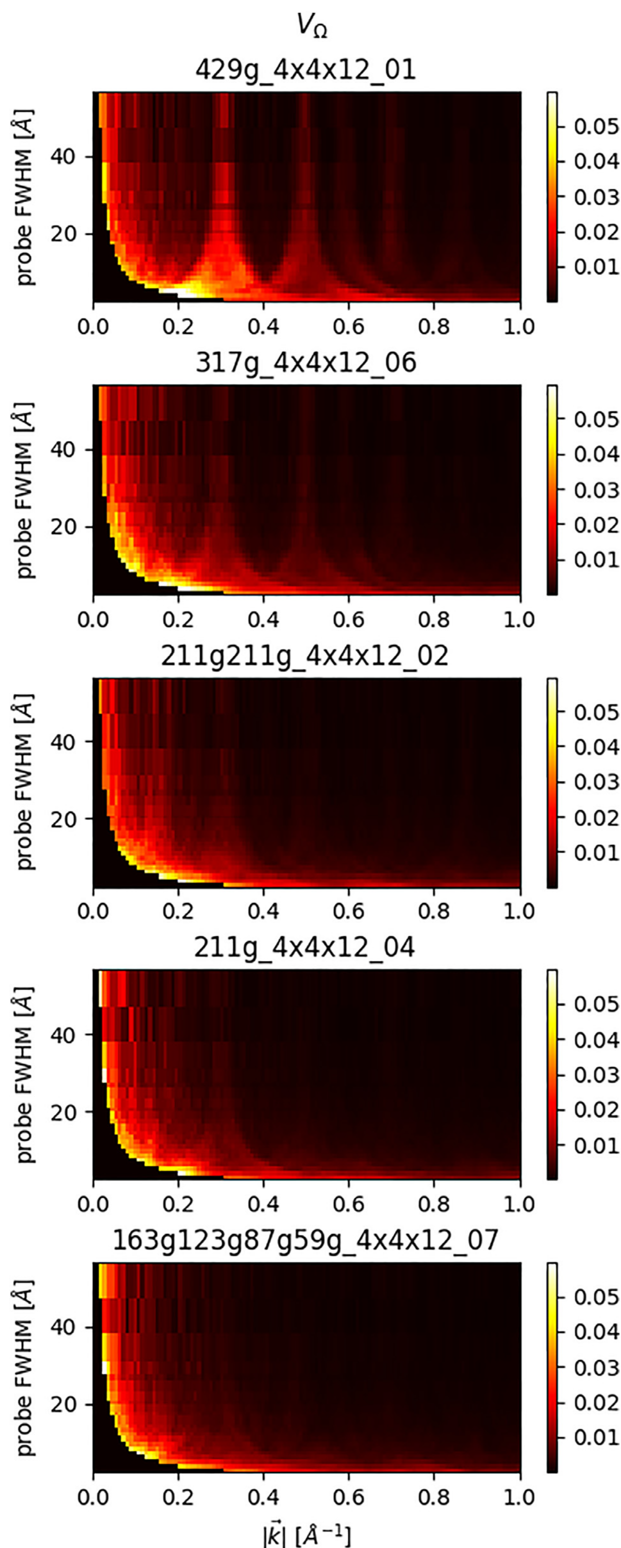

Fig. 4. Fluctuation maps for models of decreasing % crystallinity and corresponding diminishment of V_Ω peaks. FWHM is the measured full-width at half maximum of the simulated nano-beam probe, which varies inversely with both Q and the convergent beam diffraction disc diameter. (For interpretation of the references to colour in this figure legend, the reader is referred to the web version of this article.)

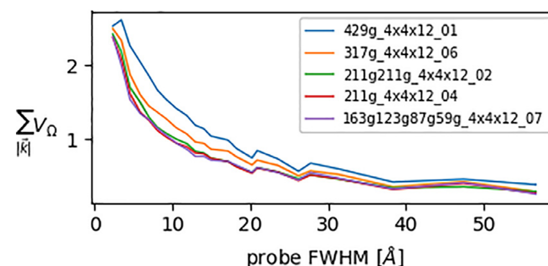

Fig. 5. Cumulative intensity of V_Ω as a function of probe size. Peaks for probe widths greater than 20 Å are due to probe artifacts caused by periodic boundary conditions. (For interpretation of the references to colour in this figure legend, the reader is referred to the web version of this article.)

3.4. Convergence

To impart confidence in the accuracy of any simulation, it is important to identify the parameter resolution requirements for obtaining sufficiently accurate results. For MS–STEM–FEM, these parameters are the number of pixels per wave-function domain dimension, the number of slices into which the model is projected, and the beam raster pattern.

Fig. 6(a) shows that for our models containing Ge atoms, domain discretizations of greater than 4.7 pixels per Angstrom yield diminishing improvements which are difficult to discern. This value may prove to be sensitive to material composition due to varying atomic potential profiles.

Simulations of a fixed area using a varying number of raster points yielded Fig. 6(b), from which it is clear that a 10 × 10 grid of 100 raster points is sufficient for our model area of 100 Å^2 when using a probe FWHM of 17Å. Inclusion of additional raster points with increasing overlap between probe areas made no difference in the resulting V_Ω curve.

Fig. 6(c) shows that using a slice thickness of less than 10–20 Å produces nearly indistinguishable results for V_Ω simulations of our models. This thickness is substantially greater than slice thicknesses recommended for multi-slice HRTEM simulations (≈1 Å) [9], and allows for gains in performance by projecting greater model thicknesses into fewer slices.

3.5. Model thickness and dynamical scattering

As indicated by Fig. 6(c), projecting the entire sample thickness into a single 340 Å slice (a kinematical approximation) will introduce errors, which previously might have been attributed to dynamical scattering. To identify the extent to which dynamical scattering influences FTEM measures we compare V_Ω simulated using models of varying thickness obtained by either duplication or extension in Fig. 7. Models constructed by extension follow the algorithm in Section 2.5, whereas models obtained by duplication simply duplicate the positions of a 429g_4 × 4 × 4 model extension along the beam direction to obtain the desired thickness.

Differences in scattering from models of varying thickness obtained by extension are attributable to both dynamical diffraction and the inclusion of a greater variety of scattering conditions in the additional layers (Fig. 7(a)), while differences in scattering from structures of increasing duplicity along the beam direction (Fig. 7(b)) are attributable only to dynamical scattering since the additional layers do not introduce scattering conditions which are not already included in the preceding layers. Although Fig. 6(c) might be interpreted as suggesting that dynamical scattering has a substantial influence on FTEM, Fig. 7(b) shows that it is limited. Variation in the curves of Fig. 6(c) could instead

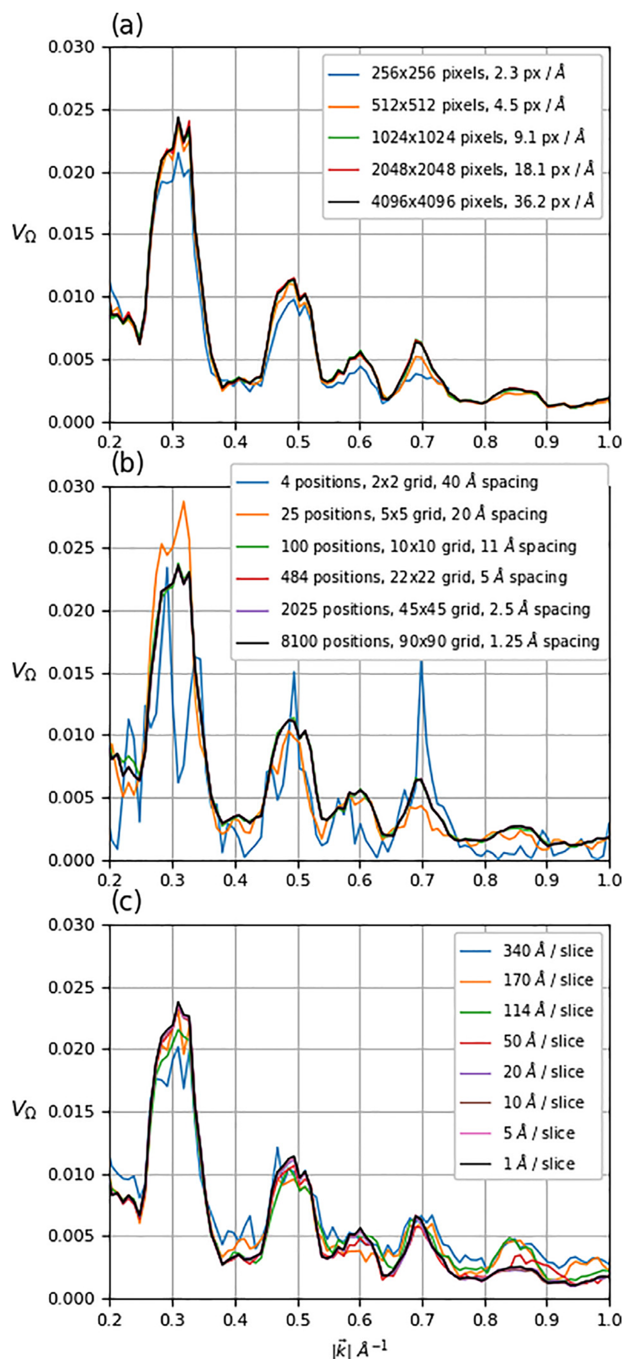

Fig. 6. Convergence of V_Ω with respect to (a) pixel resolution, (b) raster positions, and (c) minimum slice thickness parameters for a 429g_4 × 4 × 12 paracrystalline model of Ge. (For interpretation of the references to colour in this figure legend, the reader is referred to the web version of this article.)

be attributed to additional scattering conditions introduced by artificial proximity of distant atoms which are projected into a single slice.

The cause for V_Ω to diminish with thickness in experimental measurements may be an increasing variety of scattering conditions or crystallite rotations and translations, which is represented by Fig. 7(a). Simulation of samples thicker than the minimum slice thickness of approximately 20–50 Å thus require a greater number of atomic coordinates and efficient performance scaling with the number of atoms in a model.

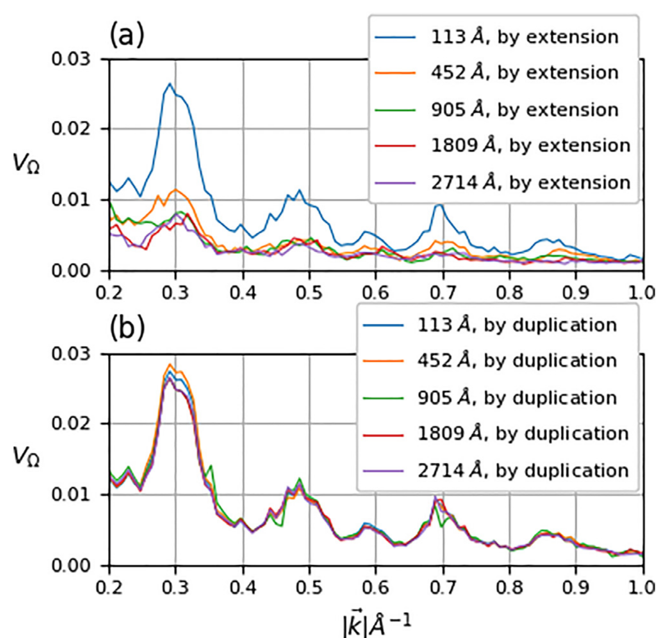

Fig. 7. V_Ω trend with model thickness obtained by (a) extending a 429g model as in Section 2.5, and (b) duplication of a 429g_4 × 4 × 4 paracrystalline model along beam propagation direction a sufficient number of times to obtain the annotated thicknesses. (For interpretation of the references to colour in this figure legend, the reader is referred to the web version of this article.)

3.6. Performance scaling

The search for models whose simulated FTEM matches with experiment may require many FTEM simulations of candidate models, and is thus particularly sensitive to FTEM simulation performance. Parallel execution using the Message Passing Interface (MPI) communication protocol helps to reduce the run-time cost and take advantage of high-performance computing clusters.

A strong-scaling study of MS–STEM–FEM is shown in Fig. 8 which used a cluster whose nodes each contain sixteen 2.6 GHz processors to calculate the same problem while varying number of processors. The speed-up of the current implementation, t_1/t, remains close to an ideal linear halving until internodal communication begins to impart a delay

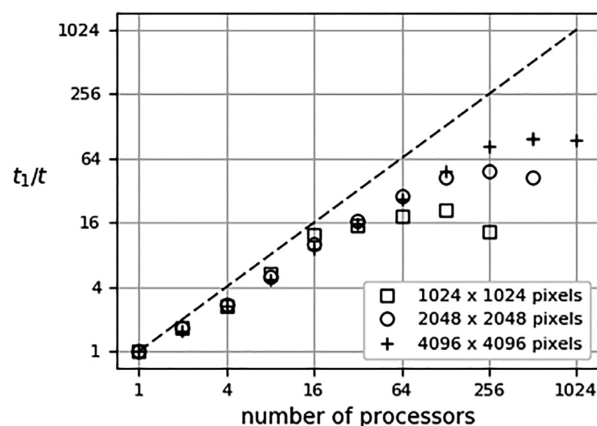

Fig. 8. Log-log plot showing speed-up of wall-clock computation time relative to the single processor computation time t_1. The dashed line represents an ideal halving of computational time when the number of processors is doubled. The number of pixels in the domain discretization are shown to affect the extent to which additional nodes contribute to improving computational time speed-up, the optimal being approximately 1/16th of the number of pixels in the x-direction.

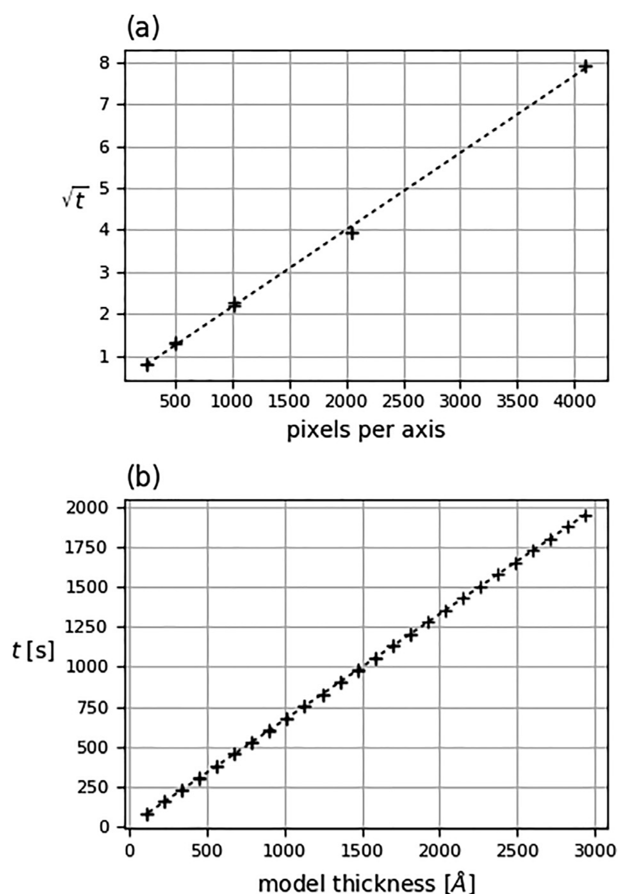

Fig. 9. Computational time scaling with respect to model dimensions. (a) linear fit of the square root of time as a function of pixels per surface side indicates quadratic scaling with area of a square model surface. (b) linear scaling with respect to model thickness using a fixed minimum slice thickness with 1024 pixels per slice side on 16 processors having 2.6 GHz clock speed.

when using more than sixteen processors. Speed-up continues to increase with additional processors until reaching approximately one sixteenth of the number of pixels in the discretized domain which is being split among nodes. The current implementation cannot scale to processor counts greater than the number of pixels in the x-direction due to the use of FFTW.

Established software is notably limited in the size of models which may be practically simulated, limiting typical amorphous constructions to volumes which are far smaller than what is sampled in an FTEM experiment. To identify model dimensions to which MS–STEM–FEM is sensitive and demonstrate that models of thickness comparable to experiment are within reach, a study of the performance scaling of MS–STEM–FEM in response to model scaling is given in Fig. 9.

Fig. 9 shows the results of two weak-scaling studies in which the size of the computational problems increased with the number of processors. Fig. 9(a) presents a linear fit of the square root of wall-clock time as a function of pixels per domain axis. This fitting indicates that MS–STEM–FEM scales quadratically with total number of pixels in the model area perpendicular to beam propagation. Fig. 9(b) shows that MS–STEM–FEM scales linearly with the model thickness along the beam propagation direction given fixed slice thicknesses. In comparison, codes based on a kinematic diffraction approximation like FEMSIM scale quadratically with number of atoms added along any direction [6]. MS–STEM–FEM suffers such a quadratic scaling only if additional atoms require expansion of the area perpendicular to the beam, while expansion of the model thickness scales linearly at worst. Simulation of model thicknesses comparable to experiment are thus made more practical by the multislice method of MS–STEM–FEM.

4. Conclusions

MS–STEM–FEM has been validated by adapting existing paracrystalline models and comparing their simulated measures to experimental STEM–FEM measurements. Favorable agreement with experiment was shown for low-frequency $V_\Omega(\|\vec{k}\|)$ peaks. The calculations also produce high-frequency peaks which are not pronounced in the experiment but are known to occur with these paracrystalline basis models. Several other statistical measures derived from diffraction were investigated. V_Ω shows the greatest ability to distinguish between paracrystalline extensions derived from a single crystallite model, while V_{re}, $\overline{V}_r$, and Ω_{VImage} produce more easily identifiable peaks for models having smaller crystallites. Despite having demonstrated a need for minimum slice thickness to avoid a kinematical approximation, dynamical scattering has been shown to have only a minor influence on the statistical measures, which were shown to diminish with increased model thickness due to inclusion of a greater number of crystallite orientations. The software was shown to scale efficiently with number of computer processors and to work well with models of thickness comparable to those which are probed in experiment.

Acknowledgments

The authors would like to thank Geoff Campbell for helpful discussions. We thank Livermore Computing for supercomputer resources.**Funding**

This material is based upon work supported by the U.S. Department of Energy, Office of Science, Office of Workforce Development for Teachers and Scientists, Office of Science Graduate Student Research (SCGSR) program. The SCGSR program is administered by the Oak Ridge Institute for Science and Education (ORISE) for the DOE. ORISE is managed by ORAU under contract number DE-SC0014664. This work was performed in part under the auspices of the U.S. Department of Energy by Lawrence Livermore National Laboratory under Contract DE-AC52-07NA27344.

Declarations of interest

None.

Supplementary material

Supplementary material associated with this article can be found, in the online version, at doi:10.1016/j.ultramic.2018.08.001.

References

[1] S.R. Elliott, Medium-range structural order in covalent amorphous solids, Nature 354 (1991) 445.
[2] P. Voyles, D. Muller, Fluctuation microscopy in the stem, Ultramicroscopy 93 (2) (2002) 147–159, https://doi.org/10.1016/S0304-3991(02)00155-9.
[3] M.M.J. Treacy, J.M. Gibson, Variable coherence microscopy: a rich source of structural information from disordered materials, Acta Crystallographica Section A 52 (1996) 212–220, https://doi.org/10.1107/S0108767395012876.
[4] M.M.J. TREACY, J.M. GIBSON, Coherence and multiple-scattering in z-contrast images, Ultramicroscopy 52 (1) (1993) 31–53, https://doi.org/10.1016/0304-3991(93)90020-X.
[5] J. Cowley, Electron nanodiffraction methods for measuring medium-range order, Ultramicroscopy 90 (2) (2002) 197–206, https://doi.org/10.1016/S0304-3991(01)

00130-9.
[6] J.J. Maldonis, J. Hwang, P.M. Voyles, Femsim + hrmc: simulation of and structural refinement using fluctuation electron microscopy for amorphous materials, Comput. Phys. Commun. 213 (2017) 217–222, https://doi.org/10.1016/j.cpc.2016.12.006.
[7] R.K. Dash, P.M. Voyles, J.M. Gibson, M.M.J. Treacy, P. Keblinski, A quantitative measure of medium-range order in amorphous materials from transmission electron micrographs, J. Phys. Condensed Matter 15 (31) (2003), https://doi.org/10.1088/0953-8984/15/31/317.
[8] T.T. Li, S.N. Bogle, J.R. Abelson, Quantitative fluctuation electron microscopy in the stem: methods to identify, avoid, and correct for artifacts, Microsc. Microanal. 20 (5) (2014) 1605–1618, https://doi.org/10.1017/S1431927614012756.
[9] E.J. Kirkland, Advanced Computing in Electron Microscopy, second ed., Springer, 2010, https://doi.org/10.1007/978-1-4419-6533-2.
[10] E.J. Kirkland, Computation in electron microscopy, Acta Crystallogr. A Found. Adv. 72 (2016) 1–27, https://doi.org/10.1107/S205327331501757X.
[11] J. Gibson, M. Treacy, Fluctuation microscopy analysis of amorphous silicon models, 70th Birthday of Robert Sinclair and 65th Birthday of Nestor J. Zaluzec PICO 2017 - Fourth Conference on Frontiers of Aberration Corrected Electron Microscopy, 176 (2017), pp. 74–79, https://doi.org/10.1016/j.ultramic.2017.01.013.
[12] N.H. Julian, 2018, https://github.com/nickjulian/ms-stem-fem.
[13] I. Free Software Foundation, Gnu general public license version 2, 1991, https://www.gnu.org/licenses/old-licenses/gpl-2.0-standalone.html.
[14] M. Frigo, S.G. Johnson, Fftw: an adaptive software architecture for the fft, Acoustics, Speech and Signal Processing, 1998. Proceedings of the 1998 IEEE International Conference on, vol. 3, (1998), pp. 1381–1384 vol.3, https://doi.org/10.1109/ICASSP.1998.681704.
[15] S.N. Bogle, P.M. Voyles, S.V. Khare, J.R. Abelson, Quantifying nanoscale order in amorphous materials: simulating fluctuation electron microscopy of amorphous silicon, J. Phys. Condensed Matter 19 (45) (2007), https://doi.org/10.1088/0953-8984/19/45/455204. FEI Co; US Natl Sci Fdn.
[16] T.T. Li, L.B.B. Aji, T.W. Heo, M.K. Santala, S.O. Kucheyev, G.H. Campbell, Effect of medium range order on pulsed laser crystallization of amorphous germanium thin films, Appl. Phys. Lett. 108 (22) (2016) 221906, https://doi.org/10.1063/1.4953153.
[17] G.T. Barkema, N. Mousseau, High-quality continuous random networks, Phys. Rev. B 62 (8) (2000) 4985–4990, https://doi.org/10.1103/PhysRevB.62.4985.
[18] A. Rezikyan, Z.J. Jibben, B.A. Rock, G.P. Zhao, F.A.M. Koeck, R.F. Nemanich, M.M.J. Treacy, Speckle suppression by decoherence in fluctuation electron microscopy, Microsc. Microanal. 21 (6) (2015) 1455â1474, https://doi.org/10.1017/S1431927615015135.
[19] F. Yi, P. Voyles, Effect of sample thickness, energy filtering, and probe coherence on fluctuation electron microscopy experiments, Ultramicroscopy 111 (8) (2011) 1375–1380, https://doi.org/10.1016/j.ultramic.2011.05.004.
[20] J. Gibson, M. Treacy, P. Voyles, Atom pair persistence in disordered materials from fluctuation microscopy, Ultramicroscopy 83 (3) (2000) 169–178, https://doi.org/10.1016/S0304-3991(00)00013-9.
[21] T. Daulton, K. Bondi, K. Kelton, Nanobeam diffraction fluctuation electron microscopy technique for structural characterization of disordered materials-application to al88-xy7fe5tix metallic glasses, Ultramicroscopy 110 (10) (2010) 1279–1289, https://doi.org/10.1016/j.ultramic.2010.05.010.